Neoplasia • Vol. 7, No. 3, March 2005, pp. 263–270 263

www.neoplasia.com

Utilizing Optical Tomography with Ultrasound Localization to Image Heterogeneous Hemoglobin Distribution in Large Breast Cancers[1]

Quing Zhu, Scott H. Kurtzman†, Poornima Hegde†, Susan Tannenbaum†, Mark Kane*, Minming Huang*, Nan Guang Chen*, Bipin Jagjivan† and Kristen Zarfos†*

*University of Connecticut, 371 Fairfield Road, U1157, Storrs, CT 06269, USA; †University of Connecticut Health Center, 263, Farmington, CT 06030, USA

Abstract

PURPOSE: **Angiogenesis in advanced breast cancers is highly distorted and heterogeneous. Noninvasive imaging that can monitor angiogenesis may be invaluable initially for diagnosis and then for assessing tumor response to treatment. By combining ultrasound (US) and near-infrared (NIR) optical imaging, a reliable new technique has emerged for localizing and characterizing tumor angiogenesis within the breast.** ***METHODS:*** **This new technique employs a commercial US transducer coupled with an array of NIR optical fibers mounted on a hand-held probe. The US image is used for lesion localization and for guiding optical imaging reconstruction. Optical sensors are used for imaging tumor total hemoglobin distribution, which is directly related to tumor angiogenesis.** ***RESULTS:*** **Six large breast carcinomas were studied and microvessel density count was then performed on tissue samples obtained from these cancers. Two patients had locally advanced breast cancers and received neoadjuvant chemotherapy for 3 months. In one patient, before chemotherapy, the total hemoglobin distribution showed a high concentration at the cancer periphery; the distribution was later confined to the core area after 3 months of treatment. In another patient, as treatment progressed, the maximum hemoglobin concentration decreased from 255.3, to 147.5, to 76.9 μmol/l with an associated reduction in spatial extension. The other four patients had cancers of 2.0 to 3.0 cm in size and were imaged either at the time of core biopsy or definitive surgery. The histologic microvessel density counts from these tumor samples correlate to hemoglobin distributions with a correlation coefficient of 0.64 (*$P < .05$*). *CONCLUSION:** **These initial results suggest that this new imaging technique may have great potential in imaging the heterogeneous vascular distribution of larger breast cancers *in vivo* and in monitoring treatment-related changes in angiogenesis during chemotherapy.**

Neoplasia (2005) **7,** 263–270

Keywords: Tumor angiogenesis, optical tomography, ultrasound, breast disease, tumor hypoxia.

Introduction

Noninvasive functional imaging of breast cancer presents a unique and worthwhile challenge. Optical tomography using near-infrared (NIR) diffused light offers great potential as a method for monitoring tumor hemoglobin distribution [1–4], which is directly related to the vascular component of tumors. Angiogenesis is a key process for tumor growth and metastasis. The use of this NIR method also provides direct insights into tumor metabolism and tumor hypoxia [5], which are important indicators of response to therapy. These functional parameters are potentially useful in the initial diagnosis of tumors and the assessment of tumor response to treatment in the neoadjuvant setting. Intense light scattering using NIR in tissues makes lesion localization difficult. Thus, to date, optical tomography has been limited to laboratory tests and feasibility studies [5–9]. In this report, we further describe our experience using a novel combination of ultrasound (US) and NIR to overcome the scattering obstacle.

US imaging is frequently used as an adjunct tool to mammography in differentiating cysts from solid lesions. US also plays an important role in guiding interventional procedures such as needle aspiration, core needle biopsy, and prebiopsy needle localization [10]. However, US features that occur in solid breast masses are not reliable enough to determine whether invasive evaluation is needed or noninvasive follow-up is indicated [11]. The lack of specificity of US has prompted radiologists to recommend biopsies on most solid nodules, resulting in a 70% to 90% negative biopsy rate [12].

By combining US and optical imaging, a reliable technique has emerged for localizing and characterizing lesions

Address all correspondence to: Prof. Quing Zhu, University of Connecticut, 371 Fairfield Road, U1157, Storrs, CT 06269. E-mail: zhu@engr.uconn.edu

[1]We thank the following funding agents for their support: National Institute of Health (R01EB002136), Donaghue Foundation, and Department of Defense Army Medical Research and Materiel Command (DAMD17-00-1-0217 and 17-01-1-0216).

Received 2 August 2004; Revised 26 September 2004; Accepted 28 September 2004.

DOI 10.1593/neo.04526

within the breast [13–16]. The technique is implemented by simultaneously deploying optical sensors and a commercial US transducer mounted on a hand-held probe, and utilizing coregistered lesion structure information provided by US to improve the inverse optical imaging reconstruction. Results have shown that early-stage invasive breast cancers may be separated from benign lesions by their significantly higher total hemoglobin concentration [16].

The process of angiogenesis is complex, resulting in a highly distorted and heterogeneous distribution of blood vessels in advanced cancers [17]. This distorted distribution is dependent on angiogenic factors [18] and related to the incorporation of existing host blood vessels into tumors and the creation of tumor microvessels. Blood flow through these tumor vessels is heterogeneous. Some areas have high flow; others have slower flow and develop necrosis [19]. Tumors with relatively poor blood perfusion may not receive adequate delivery of systemic therapy. This lack of perfusion may be a factor in the poor response to chemotherapy in some patients [20].

Although pilot studies of imaging tumor hemoglobin distributions have been conducted with optical tomography, no one has demonstrated heterogeneous hemoglobin distributions in advanced cancers. In this paper, we report the ability of optical tomography to correctly image heterogeneous hemoglobin distributions in large cancers by correlating these imaging results with histologic microvessel density counts. We also demonstrate the potential of optical tomography for monitoring tumor vascular responses to neoadjuvant chemotherapy.

Materials and Methods

A hand-held hybrid probe consists of a commercial US transducer located in the center and our NIR source detector fibers mounted in a housing, distributed at the periphery [16]. The technical aspects of the NIR imager have been described in detail previously [14]. Briefly, the imager consists of 12 pairs of dual-wavelength (780 and 830 nm) laser diodes, which are used as light sources, and their outputs are coupled to the probe through optical fibers. An additional wavelength (660 nm) is added to the system, which allows a reliable estimation of tumor oxygenation saturation. On the receiving side, eight photomultiplier tubes (PMTs) were used to detect diffusely scattered light from the tissue and eight optical fibers were used to couple detected light to the PMTs. The laser diodes' outputs were amplitude-modulated at 140 MHz and the detector outputs were demodulated to 20 kHz. The demodulated signals were further amplified and bandpass-filtered at 20 kHz. A reference signal of 20 kHz was also generated by directly mixing the detected radiofrequency (RF) signals with the RF signal generated from the oscillator. The reference signal was necessary for retrieving phase shifts. Eight detection signals and one reference were sampled and acquired into a computer simultaneously. The entire data acquisition took about 3 to 4 seconds, which was fast enough for acquiring data from patients.

The details of our dual-mesh optical imaging reconstruction algorithm have been described in Zhu et al. [15]. Briefly, the NIR reconstruction takes advantages of US localization of lesions and segments the imaging volume into a finer grid in lesion region L and a coarser grid in nonlesion background region B. In all images, a $0.5 \times 0.5 \times 0.5$-cm imaging grid was used for lesion and $1.5 \times 1.5 \times 1$ cm was used for background region. A modified Born approximation is used to relate the scattered field U_{sd} measured at each source (s) and detector pair (d) to total absorption variations at wavelength in each volume element of two regions within the sample. The matrix form of image reconstruction is given by:

$$[U_{sd}]_{M\times 1} = [\mathbf{W}_L, \mathbf{W}_B]_{M\times N}[M_L, M_B]^T_{N\times 1} \qquad (1)$$

where $\mathbf{W}_L$ and $\mathbf{W}_B$ are weight matrices for lesion and background regions, respectively, and are calculated from background absorption and reduced scattering measurements acquired at the normal contralateral breast. M_L and M_B are total absorption distribution changes of lesion and background regions, respectively. The absorption distribution at each wavelength is obtained by dividing M_L and M_B by different voxel sizes in lesion and background tissue regions. With this dual-mesh scheme, the inversion is well conditioned and the image reconstruction converges in a few iterations.

Because the major chromophores are deoxygenated (deoxyHb) and oxygenated (oxyHb) hemoglobin in the wavelength range studied, we can estimate deoxyHb and oxyHb concentrations at each imaging voxel by inverting the following equations, voxel by voxel, as:

$$\begin{bmatrix} \mu_a^{\lambda_1}(r') \\ \mu_a^{\lambda_2}(r') \end{bmatrix} = \begin{bmatrix} \varepsilon_{Hb}^{\lambda_1}, \varepsilon_{HbO_2}^{\lambda_1} \\ \varepsilon_{Hb}^{\lambda_2}, \varepsilon_{HbO_2}^{\lambda_2} \end{bmatrix} \times \begin{bmatrix} deoxyHb(r') \\ oxyHb(r') \end{bmatrix} \qquad (2)$$

$$\begin{bmatrix} deoxyHb(r') \\ oxyHb(r') \end{bmatrix} = \frac{1}{\Delta} \begin{bmatrix} \varepsilon_{HbO_2}^{\lambda_2}, -\varepsilon_{HbO_2}^{\lambda_1} \\ -\varepsilon_{Hb}^{\lambda_2}, \varepsilon_{Hb}^{\lambda_1} \end{bmatrix} \times \begin{bmatrix} \mu_a^{\lambda_1}(r') \\ \mu_a^{\lambda_2}(r') \end{bmatrix} \qquad (3)$$

where $\mu_a^{\lambda_1}(r')$ and $\mu_a^{\lambda_2}(r')$ are absorption coefficients obtained at imaging voxel r', where wavelengths λ_1 and λ_2 correspond to 780 and 830 nm in our system, respectively. ε are extinction coefficients given in Cope [27]. The total hemoglobin concentration $\text{totalHb}(r') = \text{deoxyHb}(r') + \text{oxyHb}(r')$ and oxygenation saturation $Y\% = \frac{\text{oxyHb}(r')}{\text{oxyHb}(r')+\text{deoxy}(r')}100\%$ can be calculated as:

$$\text{totalHb}(r') = \frac{1}{\Delta}\Big\{\{\varepsilon_{HbO_2}^{\lambda_2} - \varepsilon_{Hb}^{\lambda_2}\}\mu_a^{\lambda_1}(r') + \{\varepsilon_{Hb}^{\lambda_1} - \varepsilon_{HbO_2}^{\lambda_1}\}\mu_a^{\lambda_2}(r')\Big\} \qquad (4)$$

and

$$Y\% = \frac{-\varepsilon_{\mathrm{Hb}}^{\lambda_2}\frac{\mu_a^{\lambda_1}(r')}{\mu_a^{\lambda_2}(r')} + \varepsilon_{\mathrm{Hb}}^{\lambda_1}}{\left(\varepsilon_{\mathrm{HbO_2}}^{\lambda_2} - \varepsilon_{\mathrm{Hb}}^{\lambda_2}\right)\frac{\mu_a^{\lambda_1}(r')}{\mu_a^{\lambda_2}(r')} - \left(\varepsilon_{\mathrm{HbO_2}}^{\lambda_1} - \varepsilon_{\mathrm{Hb}}^{\lambda_1}\right)} 100\% \quad (5)$$

where $\Delta = \varepsilon_{Hb}^{\lambda_1}\varepsilon_{HbO_2}^{\lambda_2} - \varepsilon_{HbO_2}^{\lambda_1}\varepsilon_{Hb}^{\lambda_2}$. We have found that the best two wavelengths for total hemoglobin calculation are 780 and 830 nm, and the best two wavelengths for oxygen saturation calculation are 660 and 830 nm. These wavelength pairs were used in computing total hemoglobin concentration and oxygen saturation distributions reported in the Results section.

Because US resolution is less than 1 mm in depth for a typical 7.5-MHz US transducer such as the one we used, the boundaries between cancerous and normal tissue structures can be visualized well. However, spatial extensions of larger cancers, in general, are not well resolved in US. In addition, the NIR three-dimensional data are coregistered with one of the two spatial dimensions and depth dimensions of US. Another spatial dimension is estimated by assuming symmetry of lesion. Furthermore, the optical contrast may well extend beyond the tumor periphery due to angiogenesis development. Therefore, a larger region of interest (ROI), particularly in spatial dimensions than that visualized by US, is used for finer grid lesion region in the image reconstruction. The ROI used for each patient is listed in Table 1.

Clinical studies were performed at the University of Connecticut Health Center (UCHC). The UCHC IRB committee approved the human subject protocol. Written consents were obtained from all patients. Patients with palpable and non-palpable masses that were visible on clinical US and who were scheduled for biopsy or neoadjuvant chemotherapy were enrolled as research subjects. Six patients with tumors ranging from 2.5 to 4 cm were studied. For each patient, US images and optical measurements were acquired simultaneously at multiple locations including the lesion region, a normal region of the same breast if the breast was large, and a normal symmetric region of the contralateral breast. The optical data acquired at normal region with the best linear amplitude and phase profiles were used as reference for calculating the scattered field caused by lesions. The total hemoglobin concentration maps are quantified by measuring the maximum value at each depth (layer) and the average within 50% of the maximum value. Because the hand-held probe can be easily rotated or translated, at least three coregistered US and NIR data sets were acquired at the lesion location, and the corresponding optical absorption maps as well as the total hemoglobin concentration distribution were reconstructed using the coregistered US. The data given in Table 1, column 5 (left column) are average values obtained from at least three sets of NIR images.

To correlate the imaged hemoglobin distribution with histology microvessel density, we have performed microvessel density counts. Samples obtained at biopsy or definitive surgery were used for counting. For each sample, sections 3 to 5 μm thick were stained on an immunohistochemistry slide staining system (DAKO autostainer) with factor 8/86 mouse monoclonal antibody (antihuman von Willebrand factor; DAKO Corp., Carpinteria, CA) at 1:100 dilution digested by proteinase K for 3 minutes by labeled polymers (DAKO EnVision plus) using the immunoperoxidase method. Histologic microvessel density count was assessed by immunohistochemistry as initially proposed by

Table 1. Histologic Microvessel Density Counts and Total Hemoglobin Measurements.

Cases	Biopsy Sample Location	Mvd Per 10 Fields at ×200	Surgical Sample Location	Mvd Per 10 Fields at ×200	Total Hb (Maximum/Mean)	Size-Measured ROI for NIR by US (cm) Imaging (cm)
Case 1	NA	NA	ANT	114	(75.9/54.0)	4 × 4 × 1.5; 8.4 × 8.4 × 1.9
Invasive ductal	NA	NA	POST/INF	48	(39.5/26.6)	
Case 2	ANT	61*	ANT	52	(45.9/31.6)	3 × 3 × 2.0; 9 × 9 × 2.0
Invasive ductal	POST	40*	POST	29	(42.9/30.8)	
Case 3	NA	NA	ANT	83	(146.4/106.0)	2.5 × 2.5 × 1.3; 8 × 8 × 1.6
Invasive and *in situ* ductal	NA	NA	POST	124†	(174.9/122.3)	
	NA	NA	POST/LAT	121		
Case 4	NA	NA	ANT/LAT	60†	(112.5/81.1)	3 × 3 × 1.5; 7 × 7 × 1.7
	NA	NA	ANT/MED	88		
Invasive and *in situ* ductal	NA	NA	POST/INF	152	(88.4/65.8)	
Case 5	NA	NA	ANT	111	(77.2/55.6)	4 × 4 × 2.0; 8 × 8 × 2.0
	NA	NA	POST	68	(16.1/12.9)	
Invasive ductal	ANT(LIQ)+	190	ANT(LIQ)	61		
Case 6	NA	NA	ANT	86†	(97/66.5)	2 × 2 × 1.0; 7 × 7 × 1.0
Invasive ductal	NA	NA	POST	109		

ANT, anterior; POST, posterior; LAT, lateral; MED, medial; INF, inferior.
Mvd per 10 fields at ×200: total microvessels per 10 consecutive fields at ×200 magnifications.
+LIQ, low inner quadrant.
*For case 2, NIR/US data are acquired at core biopsy; therefore, the microvessel density counts obtained at the time of core US were used in Figure 5.
† The average is used in obtaining Figure 5.

Weidner et al. [20]. The microvessel density counts were performed in 10 consecutive fields with the use of an ocular grid at ×200 magnification. The first field chosen was a hotspot (area of maximum vascular density either within the infiltrating tumor mass or at the tumor–stromal interface). Because the cancers were large, two to three separate sample blocks were selected for microvessel counts as per specimen orientation in the surgical pathology report. The performer was blinded from the NIR imaging results.

The surgeon always orients the excised specimen with sutures designating the resection margins. Tumor sampling for histologic studies demonstrates the relationship of the tumor to the designated resection margins. Because the patients were imaged from the anterior approach with the patient in supine position, orientation of the anterior and deep (posterior) locations within the optical and US images could be easily linked to the orientation of the surgical material.

The linear regression curve of microvessel density count *versus* measured maximum total hemoglobin concentration at the corresponding location was obtained from least square solutions. The correlation coefficient that reflecting the goodness of fit was computed as: $r = \frac{\text{coeff}_{xy}}{\sqrt{\text{var}_x \text{var}_y}}$, where $\text{coeff}_{xy} = \sum_{i=1}^{n}(x_i - \bar{x})(y_i - \bar{y})$, $\text{var}_x = \sum_{i=1}^{n}(x_i - \bar{x})^2$, and $\text{var}_y = \sum_{i=1}^{n}(y_i - \bar{y})^2 \cdot$ $(x_i y_i)$ is a sample point of microvessel density count and its corresponding maximum total hemoglobin concentration, and $(\bar{x}, \bar{y})$ is the mean value of the corresponding variables. The statistical significance was tested on correlation coefficients with a confidence level of 0.05.

Results

The first patient had a 4 × 4 × 1.5-cm palpable mass (Figure 1*a*) that was considered as highly suspicious for malignancy. An US-guided needle biopsy confirmed that the lesion was a poorly differentiated invasive ductal carcinoma with necrosis. The total hemoglobin concentration map shown in Figure 1*b* reveals that the distribution is highly heterogeneous. The image reveals a high concentration of hemoglobin distributed at the cancer periphery. The maximum and average hemoglobin concentrations of three layers (slices 3–5) are 90.7/56.2, 50.2/31.6, and 27.4/25.2 μmol/l, respectively. Because this cancer was considered too large for breast-conserving surgery with an acceptable cosmetic result, the patient was treated with chemotherapy in the neoadjuvant setting for 3 months. At the completion of her chemotherapy, we imaged the tumor again. Figure 1*c* is the US image of the cancer 3 months later. The cancer contrast is poor and cancer boundaries are completely unclear, probably due to treatment. Figure 1*d* is the total hemoglobin distribution. The maximum and average hemoglobin concentrations of the three layers (slices 3–5) are 73.6/52.5, 64.2/43.9, and 44.0/28.7 μmol/l, respectively. Compared with the images acquired before treatment, the spatial extension of the hemoglobin concentration is much smaller and more confined to the core area. The maximum total hemoglobin concentration is reduced by about 15 μmol/l.

To correlate the NIR images with microvessel densities, we selected two block samples obtained at breast conservation surgery marked as anterior and posterior (Figure 1*c* insertion) for microvessel counting. The total numbers of microvessels were 114 (anterior) and 48 (posterior and inferior) per 10 consecutive fields at ×200 magnification, respectively (Table 1, *case 1*). The high counts obtained at the anterior correlate with the high hemoglobin concentration shown in slice 3 of Figure 1*d*. A representative section demonstrating high microvessel density is shown in Figure 1*e*. The low counts obtained at posterior and inferior block samples correlate with the low hemoglobin concentration seen in the deeper slice 5 of Figure 1*d*.

The second patient had a 3 × 3 × 2-cm dominant mass. US showed a hypoechoic mass with irregular margins (Figure 2*a*) and the lesion was considered as highly suspicious for malignancy. Resection of the mass revealed a moderately differentiated infiltrating carcinoma with low mitotic activity. Figure 2*b* shows the total hemoglobin map; the hemoglobin concentration is low and the distribution is heterogeneous. The measured maximum total hemoglobin concentration and average of three layers (slices 4–6) are 48.0/33.7, 48.4 /33.9, and 44.4/31.8 μmol/l, respectively. The total counts of microvessels obtained from anterior and posterior core biopsy samples were 61 and 40, respectively (Table 1, *case 2*). The total counts measured from anterior and posterior tumor samples obtained at definitive surgery were 52 and 29, respectively. These low counts correlate well with the low hemoglobin concentration shown in Figure 2*b* and indicate that the tumor had a minimal vascular supply. A representative section demonstrating low microvessel density is shown in Figure 2*c*.

The third example was obtained from a patient with a diffusely swollen breast. No discrete mass was palpable. An incisional biopsy from the lower inner quadrant showed a poorly differentiated infiltrating ductal carcinoma. Positive emission tomography (PET) imaging obtained before chemotherapy treatment (Figure 3*a*) revealed a diffusely involved breast with nodal and epidural metastasis. We identified an upper quadrant mass from US and monitored total hemoglobin concentration and oxygen saturation during her neoadjuvant chemotherapy. Figure 4, *a–c* presents a US image acquired at the beginning, after four and eight cycles of chemotherapy; Figure 4, *d–f* are corresponding total hemoglobin changes, and Figure 4, *g–i* are corresponding oxygen saturation maps. The maximum hemoglobin concentration had significantly decreased from 255.3 to 147.5 to 76.9 mol/l as did the spatial extension from the beginning to the end of the treatment. High oxygen saturation was noted in the tumor initially near the chest wall region (*slices 6 and 7*, Figure 4*g*) and fell to deoxygenated levels at the time of the second scan (Figure 4, *h* and *i*). The initial incisional biopsy was in a region where there was no demonstrable mass on US so the initial microvessel count is not from the same region imaged by optical tomography shown in Figure 4*d*. Microvessel counts of surgical samples obtained from

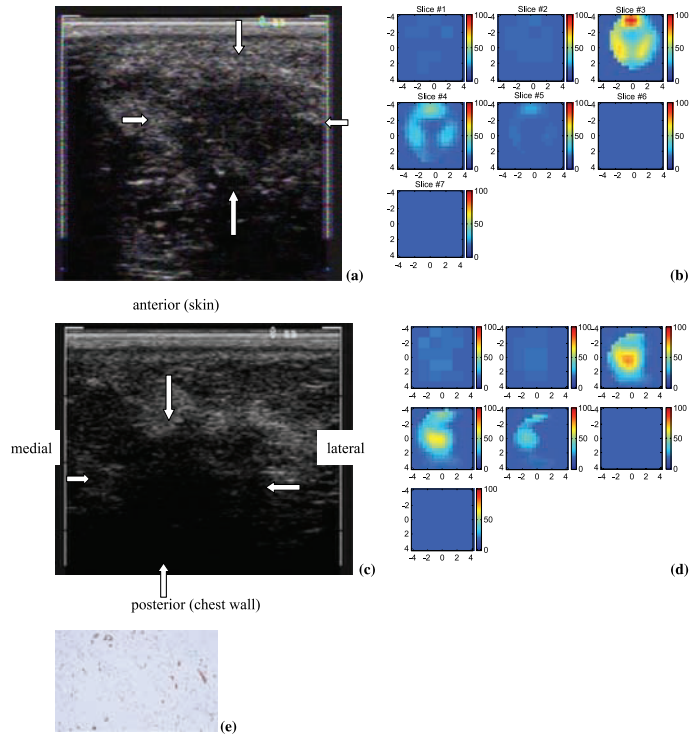

Figure 1. *(a) US image of a 4 × 4-cm high-grade invasive ductal cancer. (b) Total hemoglobin concentration of the lesion. Slice 1 is an x–y image of 9 × 9 cm obtained at 0.2 cm depth from the skin surface, and slice 7 is 3.2 cm deep toward the chest wall. The order of slices is from left to right and from top to bottom. The spacing between the slices is 0.5 cm. The vertical scale (mol/l) ranges from 0 to 100 μmol/l. (c) US image of the same cancer treated with chemotherapy for 3 months. (d) Total hemoglobin concentration of the lesion and the vertical scale (mol/l) ranging from 0 to 100 μmol/l. (e) Representative section of the infiltrating ductal carcinoma of the breast demonstrating high microvessel density (original magnification, ×200; anti–human von Willebrand factor, DAKO EnVision plus).*

anterior and posterior regions of the imaged area were 111 and 68, which correlate with higher and lower hemoglobin images seen in slices 4 and 6 of Figure 4*f*. PET imaging showed a complete response to chemotherapy (Figure 3*b*).

On completion of neoadjuvant chemotherapy, the patient underwent left modified radical mastectomy. Residual tumor was noted to be diffusely infiltrating all the quadrants of the breast as well as beneath the nipple. However, there was

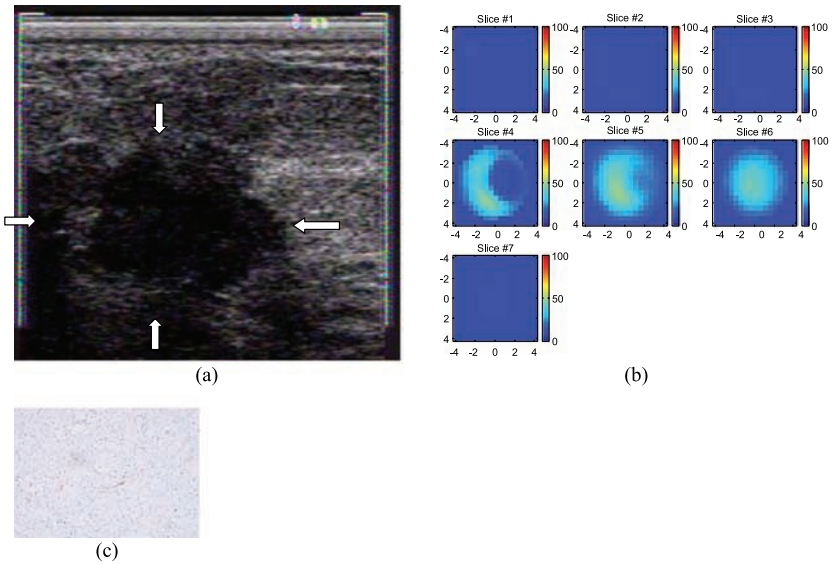

Figure 2. *(a) US image of an intermediate-grade infiltrating ductal cancer. (b) Total hemoglobin concentration of the lesion (mol/l) ranging from 0 to 100 μmol/l. Slice 1 is an x–y image of 9 × 9 cm obtained at 0.5 cm depth from the skin surface, and slice 7 is 3.5 cm deep toward the chest wall. (c) Representative section of infiltrating ductal carcinoma of the breast demonstrating low microvessel density (original magnification, ×200; anti–human von Willebrand factor; DAKO EnVision plus).*

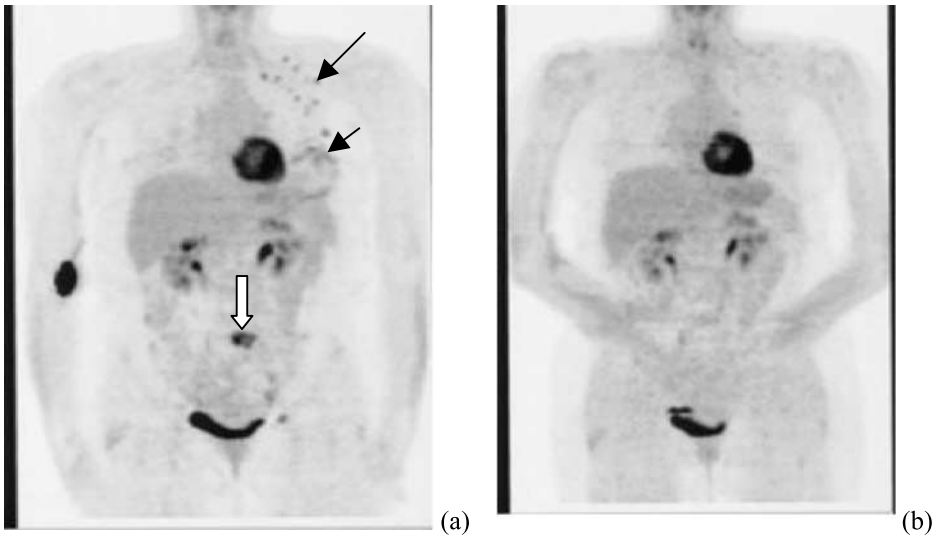

Figure 3. *PET images of a patient who presented with a diffusely swollen breast. Core biopsy revealed a high-grade infiltrating ductal cancer. (a) Image acquired before chemotherapy. The small black arrow indicates the diffuse involvement of the breast. The longer black arrow indicates positive lymph nodes (black dots). The white arrow displays an area of metastatic disease (epidural). (b) PET image acquired after eight cycles of chemotherapy, before definitive surgery. No evidence of disease remains.*

marked reduction in tumor cellularity to 5% throughout the fibrotic bed of the residual tumor.

Table 1 summarizes the results of six cases. The histology is given in column 1. Columns 2 and 3 list the location of core biopsy samples and the corresponding microvessel counts. Four cases were diagnosed with fine needle biopsy and no tumor sample was available for microvessel density counting. Columns 4 and 5 (left) provide the location of the surgical sample obtained at definitive surgery and the corresponding microvessel counts. The maximum and average hemoglobin concentrations at the corresponding depth (layer) were given in column 5 (right). The US-measured cancer size (right) at the time of the study, or at the beginning of the chemotherapy, and the ROI used for finer mesh (left) for each case are given in the last column. The data of microvessel density count (column 5, left) *versus* measured maximum total hemoglobin concentration (column 5, right) are shown in Figure 5. The linear regression curve is also given in the figure and the correlation coefficient is 0.64, which is statistically significant ($P < .05$). One data point obtained at the posterior/inferior location of case 4 was an outlier and was removed to obtain the linear regression curve.

Discussion

Optical tomography with US localization appears to have potential value in distinguishing benign from smaller malignant tumors [16]. The current study elucidates additional benefits when studying larger tumors (to map tumor vascularity and tumor hypoxia). These indices can be followed before and during therapeutic interventions. It has been shown that tumor hypoxia is related to the growth rate and chemotherapeutic responsiveness of tumors [28]. The ability to demonstrate and follow these parameters before and during therapy noninvasively could prove invaluable in choosing tailored treatments especially in the era of new drugs targeting angiogenesis.

Some of the other newer imaging techniques do not have this capability. These techniques utilized clinically and experimentally include $^{15}O-$water contrast-enhanced positron emission tomography [21], dynamic contrast-enhanced magnetic resonance imaging (MRI) [22,23], ^{99}m Tc-sestamibi contrast-enhanced single-photon emission tomography [24,25], and Doppler sonography [26]. The first three techniques require rather expensive systems and may only be used at the beginning and end of chemotherapy, leaving the entire treatment period completely unmonitored. The Doppler sonography is limited to imaging large blood vessels. Compared with Doppler sonography, which visualizes larger blood vessels, optical tomography images tumor microvessel density, which is directly related to tumor angiogenesis distributions. Furthermore, NIR systems are cost-effective, portable, and easily coupled to clinical US systems for repeated imaging.

Although pilot studies of imaging tumor hemoglobin distributions have been conducted with optical tomography, no one has obtained heterogeneous hemoglobin distributions in advanced cancers and demonstrated its correlation with histologic microvessel density counts. In this paper, we report the first heterogeneous hemoglobin distributions of large cancers imaged by optical tomography, and we show that the hemoglobin distribution correlates to histologic microvessel density counts. We also demonstrate the potential of optical tomography to monitor the response of tumors, more specifically their vascularity, to neoadjuvant chemotherapy.

For each individual patient, except case 4, the maximum and average total hemoglobin concentrations measured at the top and bottom layers correlate to the histologic microvessel density counts obtained at anterior and posterior samples, respectively. The NIR data from case 4 were

different from the others because the imaging was done 8 days after the biopsy at the time of the patient visit. Postbiopsy wound healing may impact on vascularity measured by NIR. NIR scans of other patients were done prior to any invasive procedures (cases 1–3 and 5) or 3 months later after initial fine needle biopsy (case 6). In addition, this patient was completing her first trimester pregnancy at the time of the study. The larger variation in total counts at different tumor locations may partially relate to the inherent heterogeneity of breast tissues and tumors, and the differential distribution of angiogenesis in the viable and schirrous regions. Nevertheless, the relatively higher counts obtained from the three sample blocks correlate to a large extent to the high hemoglobin distribution.

In the reported studies, we have used bulk absorption and reduced scattering coefficients obtained from the fitting results of normal breasts to compute the weight matrices. We reconstructed the absorption variations of both lesion and background, and then computed the total hemoglobin distribution from the absorption changes. Optical scattering changes also contribute to the measured perturbations. We have attempted to reconstruct both absorption and reduced scattering changes simultaneously, but have not been successful with the modified Born approximation. The main reason is that the weight matrices of absorption and scattering coefficients are not on the same order. By appropriately scaling the weight matrices as reported in Huang et al. [29], we can improve the simultaneous reconstruction for phantom targets but not reliably for all clinical cases. Currently, we are investigating simultaneous reconstruction using the finite element method. We are also investigating the time-resolved method [30] because scattering inhomogeneities mainly influence photons with rather short propagation paths [31,32]. However, a study of 13 optically visible cancers using the time-resolved method has shown that 12 cases have presented 10% to 175% relative changes in absorption between tumors and surrounding tissues [8]. Only two cases have shown relative scattering heterogeneity changes from 10% to 15%, and one case has shown changes of 25% from the bulk value. Therefore, we believe that the results reported here mainly represent the changes of lesion absorption, and the correlation between the total hemoglobin

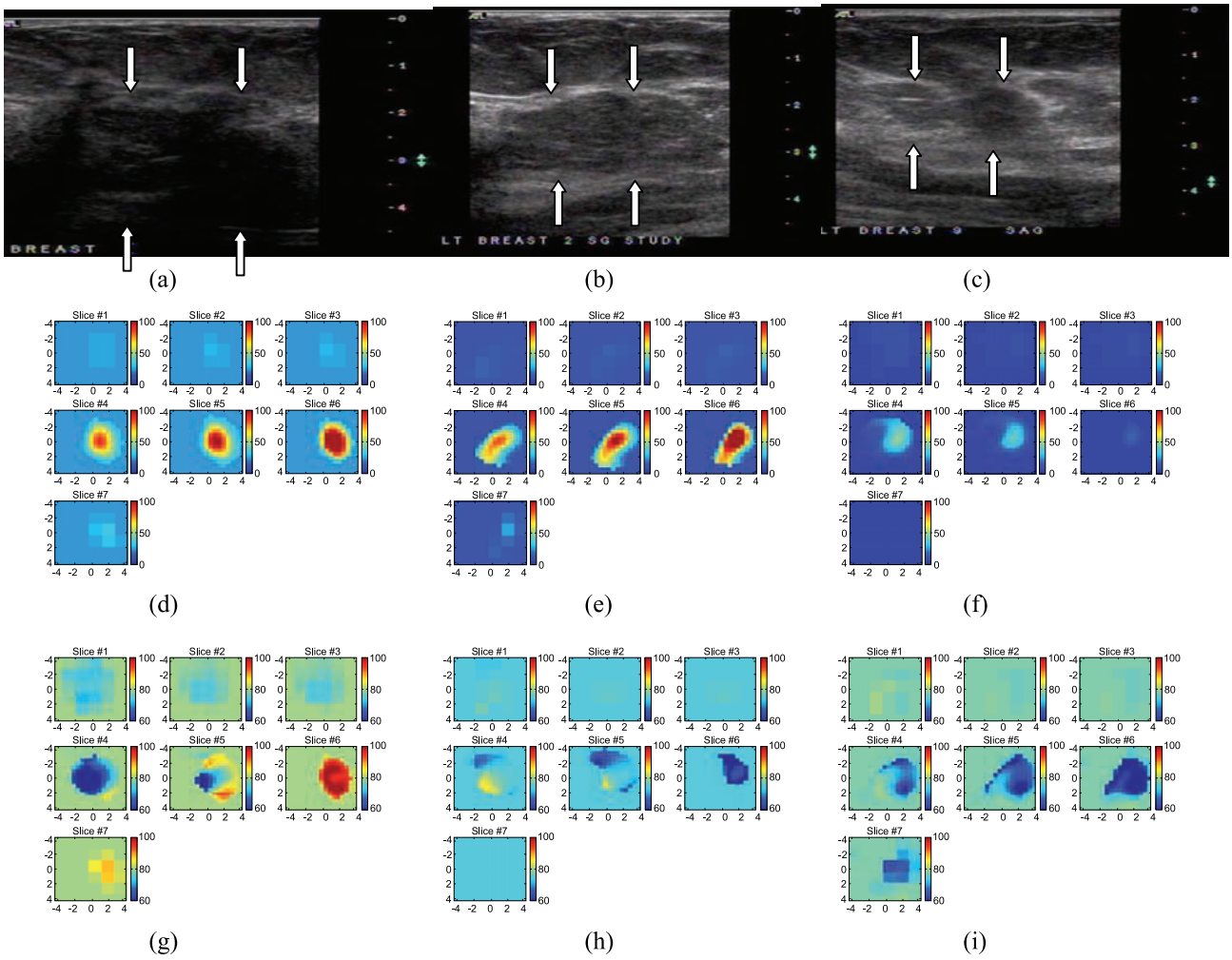

Figure 4. *Corresponding US images acquired at the beginning (a), after four cycles (b), and after eight cycles (c) of chemotherapy. (d–f) Corresponding NIR hemoglobin concentrations. (g–i) Oxygen saturation maps. Slice 1 is an x–y image of 9 × 9 cm obtained at 0.5 cm depth from the skin surface, and slice 7 is 3.5 cm deep toward the chest wall. The slices in (d)–(I) are numbered from left to right and from top to bottom.*

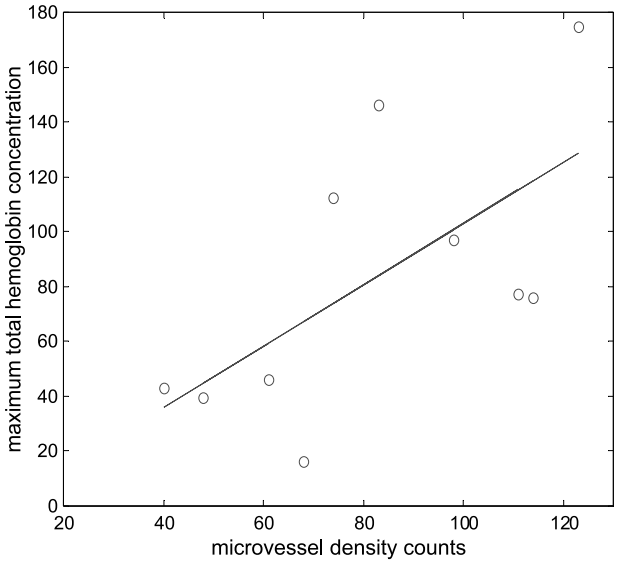

Figure 5. *Microvessel density counts obtained at anterior and posterior surgical samples versus measured maximum total hemoglobin concentration at the corresponding layers. Linear regression analysis obtained a 0.64 correlation coefficient, which is statistically significant (P < .05).*

concentration and the microvessel counts provides further evidence of this.

Acknowledgements

The authors thank Ellen Oliver (surgical nurse, Cancer Center) and Deborah McMahon (coordinator, Department of Radiology, UCHC) for their continuous efforts in the scheduling of patients. The UCHC ultrasound technologists Brenda Cameron, Debra Perusse, and Natalie Brown (Department of Radiology) were extremely helpful in assisting US data acquisition and patient scanning.

References

[1] Yodh A and Chance B (1995). Spectroscopy and imaging with diffusing light. *Phys Today* **48,** 34–40.

[2] Tromberg B, Shah N, Lanning R, Cerussi A, Espinoza J, Pham T, Svaasand L, and Butler J (2000). Non-invasive *in vivo* characterization of breast tumors using photon migration spectroscopy. *Neoplasia* **2** (1:2), 26–40.

[3] Chance B (1998). Near-infrared images using continuous, phase-modulated, and pulsed light with quantitation of blood and blood oxygenation. *Ann NY Acad Sci* **838,** 29–45.

[4] Alfano R, Demos S, and Gayen SK (1997). Advances in optical imaging of biomedical media. *Ann NY Acad Sci* **820,** 248–270.

[5] Ntziachristos V, Yodh A, Schnall M, and Chance B (2000). Concurrent MRI and diffuse optical tomography of breast after indocyanine green enhancement. *Proc Natl Acad Sci* **97** (6), 2267–2772.

[6] Franceschini MA, Moesta KT, Fantini S, Gaida G, Gratton E, Jess H, Mantulin WW, Seeber M, Schlag PM, and Kaschke M (1997). Frequency-domain techniques enhance optical mammography: initial clinical results. *Proc Natl Acad Sci* **94,** 6468–6473.

[7] Pogue B, Poplack SP, McBride TO, Wells WA, Osterman K, Osterberg U, and Paulsen KD (2001). Quantitative hemoglobin tomography with diffuse near-infrared spectroscopy: pilot results in the breast. *Radiology* **218,** 261–266.

[8] Grosenick D, Moesta KT, Wabnitz H, Mucke J, Stroszczynski C, Macdonald R, Schlag PM, and Rinneberg H (2003). Time-domain optical mammography: initial clinical results on detection and characterization of breast tumors. *Appl Opt* **42** (16), 3170–3186.

[9] Jiang H, Xu Y, Iftimia N, Eggert J, Klove K, Baron L, and Fajardo L (2001). Three-dimensional optical tomographic imaging of breast in a human subject. *IEEE Trans Med Imaging* **20** (12), 1334–1340.

[10] Fornage BD, Coan JD, and David CL (1992). Ultrasound-guided needle biopsy of the breast and other interventional procedures. *Radiol Clin North Am* **30,** 167–185.

[11] Jackson VP (1995). The current role of ultrasonography in breast imaging. *Radiol Clin North Am* **33,** 1161–1170.

[12] Rahbar G, Sie AC, Hansen GC, Prince JS, Melany ML, Reynolds HE, Jackson VP, Sayre JW, and Bassett LW (1999). Benign versus malignant solid masses: US differentiation. *Radiology* **213,** 889–894.

[13] Zhu Q, Durduran T, Holboke M, Ntziachristos V, and Yodh A (1999). Imager that combines near-infrared diffusive light and ultrasound. *Opt Lett* **24** (15), 1050–1052.

[14] Chen NG, Guo PY, Yan SK, Piao DQ, and Zhu Q (2001). Simultaneous near-infrared diffusive light and ultrasound imaging. *Appl Opt* **40** (34), 6367–6380.

[15] Zhu Q, Chen NG, and Kurtzman S (2003). Imaging tumor angiogenesis using combined near-infrared diffusive light and ultrasound. *Opt Lett* **28** (5), 337–339.

[16] Zhu Q, Huang MM, Chen NG, Zarfos K, Jagjivan B, Kane M, Hegde P, and Kurtzman SH (2003). Ultrasound-guided optical tomographic imaging of malignant and benign breast lesions. *Neoplasia* **5** (5), 379–388.

[17] Mankoff DA, Dunnwald LK, Gralow JR, Ellis GK, Charlop A, Lawton TJ, Schubert EK, Tseng J, and Livington RB (2002). Blood flow and metabolism in locally advanced breast cancer: relationship to response to therapy. *J Nucl Med* **43** (4), 500–509.

[18] Vaupel P, Kallinowski F, and Okunieff P (1989). Blood flow, oxygen and nutrient supply, and metabolic microenvironment of human tumors: a review. *Cancer Res* **49,** 6449–6465.

[19] Jain RK (1991). Hemodynamic and transport barriers to the treatment of solid tumors. *Int J Radiat Biol* **60,** 85–100.

[20] Weidner N, Semple JP, Welch WR, and Folkman J (1991). Tumor angiogenesis and metastasis—correlation in invasive breast carcinoma. *N Engl J Med* **324** (1), 1–8.

[21] Wilson CBJH, Lammertsma AA, McKenzie CG, Sikora K, and Jones T (1992). Measurements of blood flow and exchanging water space in breast tumors using positron emission tomography: a rapid and non-invasive dynamic method. *Cancer Res* **52,** 1592–1597.

[22] Abraham DC, Jones RC, Jones SE, Cheek JH, Peters GN, Knox SM, Grant MD, Hampe DW, Savino DA, and Harms SE (1996). Evaluation of neoadjuvant chemotherapeutic response of locally advanced breast cancer by magnetic resonance imaging. *Cancer* **78,** 91–100.

[23] Gilles R, Guinebretiere JM, Shapeero LG, Lesnik A, Contesso G, and Sarrazin D (1993). Assessment of breast cancer recurrence with contrast-enhanced subtraction MR imaging: preliminary results in 26 patients. *Radiology* **188,** 473–478.

[24] Maini CL, Tofani A, Sciuto R, Semprebene A, Cavaliere R, Mottolese M, Benevolo M, Ferranti F, Grandinetti ML, Vici P, Lopez M, and Botti C (1997). Technetium-99m-MIBI scintigraphy in the assessment of neoadjuvant chemotherapy in breast carcinoma. *J Nucl Med* **38,** 1546–1550.

[25] Mankoff DA, Dunnwald LK, Gralow JR, Ellis GK, Drucker MJ, and Livingston RB (1999). Monitoring the response of patients with locally advanced breast carcinoma to neoadjuvant chemotherapy using [technetium-99m]sestamibi scintimammography. *Cancer* **85,** 2410–2423.

[26] Kedar RP, Cosgrove DO, Smith IE, Mansi JL, and Bamber JC (1994). Breast carcinoma: measurement of tumor response to primary medical therapy with color flow Doppler imaging. *Radiology* **190,** 825–830.

[27] Cope M (1991). PhD Dissertation University College of London, London.

[28] Vaupel P, Schlenger K, Knoop C, and Hockel M (1991). Oxygenation of human tumors: evaluation of tissue oxygen distribution in breast cancers by computerized O_2 tension measurements. *Cancer Res* **51,** 3316–3322.

[29] Huang MM, Xie TQ, Chen NG, and Zhu Q (2003). Simultaneous reconstruction of absorption and scattering maps with ultrasound localization. *Appl Opt* **42** (19), 4102–4114.

[30] Chen NG and Zhu Q (2002). Time-resolved optical measurements with spread spectrum excitations. *Opt Lett* **127** (20), 806–808.

[31] Gandjbakhche AH, Chernomordik V, Hebden JC, and Nossal R (1998). Time-dependent contrast functions for quantitative imaging in time-resolved transillumination experiments. *Appl Opt* **37,** 1973–1981.

[32] Hall DJ, Hebden JC, and Delpy DT (1997). Imaging very-low-contrast object in breastlike scattering media with a time-resolved method. *Appl Opt* **36,** 7270–7276.